



Multi-site intermetallic Ni₃Mo effectively boosts selective ammonia synthesis

H.Y. Zhou^{a,b,1}, Y.B. Qu^{a,1}, Y.C. Fan^b, Z.L. Wang^a, X.Y. Lang^{a,*}, J.C. Li^a, Q. Jiang^{a,*}

^a Key Laboratory of Automobile Materials, Ministry of Education, and School of Materials Science and Engineering, Jilin University, Changchun 130022, China

^b PetroChina Shenzhen New Energy Research Institute, Shenzhen 518000, China

ARTICLE INFO

Keywords:

Nitrogen reduction reaction
Ammonia synthesis
Electrocatalyst design
Intermetallic compound
DFT calculation

ABSTRACT

Carbon-free electrocatalytic nitrogen reduction reaction (NRR) offers an environmentally sustainable alternative to the current Haber-Bosch process in the industry. However, this process is still limited by the scaling relations and the competitive hydrogen evolution reaction (HER). Using the density functional theory, we theoretically present a strategy for separating the active sites of the N₂ activation and the hydrogenation of NH_z (z = 1, 2) intermediates on the Ni₃Mo surface, which subtly optimized the adsorption of intermediates and bypasses the scaling relations, achieving efficient NRR with an ultralow limiting potential of −0.19 V. Besides, the Ni₃Mo greatly protects the active centers of NRR from competitive H adsorption and retard the undesired HER, enabling highly selective NH₃ synthesis. The above theoretical designs are supported by proof-of-concept experimental results, where Ni₃Mo exhibits excellent NRR performance with the NH₃ yield rate of 17.35 ± 0.3 μg h^{−1} cm^{−2} at −0.35 V.

1. Introduction

Ammonia (NH₃), an essential feedstock in the production of fertilizers and common chemicals, is crucial for the development of human society and the global economy [1]. Besides, NH₃ has also been regarded as a promising hydrogen energy carrier in a sustainable future due to its zero carbon content, high hydrogen content (17.6 wt%) and easier liquefaction than H₂ [2]. Currently, the industrial NH₃ synthesis heavily relies on the century-old Haber-Bosch (H-B) process, which is normally driven by fossil fuel and operates at high temperatures (400–500 °C) and pressures (10–30 MPa), resulting in massive energy consumption and detrimental CO₂ emission [3]. Electrochemical nitrogen reduction reaction (NRR) driven by renewable electricity is considered a clean and sustainable replacement, which generates NH₃ directly from N₂ and water with help of electrocatalysts under mild conditions. Additionally, electrochemical NRR is thermodynamically predicted to be more energy-efficient than the H-B process by ~20% [4,5]. Despite the above merits, there remain significant challenges to developing desirable NRR electrocatalysts, which are as follows: (i) the difficult adsorption and activation of inert N₂ molecule with extraordinarily stable N≡N bond (941 kJ/mol), (ii) the competitive adsorption of N₂ and H at the active

sites as well as (iii) the inevitable competitive hydrogen evolution reaction (HER) [6–8].

Transition metal (TM)-based electrocatalysts have been regarded as the promising candidate due to their partially occupied *d* orbitals with abundant electron density, allowing acceptance of the σ-electrons from N₂ and meanwhile the injection of *d*-electrons into the N₂-π* orbitals for activation, which is acknowledged as the "acceptance-donation" mechanism [9]. However, proton adsorption is thermodynamically more favorable than N₂ adsorption on these TM sites, which would hinder the initiation of NRR [5]. Among these TM species, owing to the desirable half-filled 4*d*⁵ electronic configurations, Mo exhibits strong adsorption of N₂ and could effectively activate the inert N≡N bond, implying a high N₂ affinity [10,11]. Thus, a wide variety of Mo-related chalcogenides, carbides, nitrides and oxides have been investigated as potential electrocatalysts for NRR [12–15]. Unfortunately, based on the scaling relations, the NRR process on catalysts with strong N₂ adsorption is generally hindered by the hydrogenation of NH_z intermediates (z = 1, 2), giving rise to a lower activity than HER [16–18]. As a result, most electrons and protons in the solution contribute to HER rather than NRR, limiting the selectivity towards NH₃. Therefore, an ideal NRR electrocatalyst should display relatively strong N₂ affinity and low energy

* Corresponding authors.

E-mail addresses: xylang@jlu.edu.cn (X.Y. Lang), jiangq@jlu.edu.cn (Q. Jiang).

¹ These authors contributed equally to this work.

barrier for NH_3 synthesis, while the key of latter is the selective stabilization of the reaction intermediates.

Constructing multi-site electrocatalysts via alloying is a promising strategy to circumvent the scaling relations in NRR [19]. Alloying could effectively combine unique advantages between the heterogeneous metal species for regulating the geometric and electronic structures [20, 21]. Recently, Fan et al. reported that the nanoporous NiSb alloy exhibits great activity and selectivity for NRR at low potential because the alloying induces the separation of binding sites for proton and N_2 molecule [22]. Furthermore, the intermetallic compounds have well-defined stoichiometry and ordered crystal structures with robustly stable and uniform active sites implanted into the lattice framework, allowing for durable catalytic performance and a better understanding of the intrinsic reaction mechanism [20,23]. Meanwhile, intermetallic compounds could be experimentally synthesized easily via phase diagrams. The high-density active sites can be obtained on the surface of nanoporous intermetallic compounds [24]. Following this line of thought, Ni, which possesses a weak interaction with N_2 , is an appropriate metal for alloying with Mo to regulate the adsorption/activation of N_2 and the destabilization of NH_x intermediates during the NRR process. Moreover, Ni metal has a relatively strong H affinity, which prevents the active Mo sites from H blocking for achieving preferential N_2 adsorption and activation [25].

Hence, we report an intriguing strategy to circumvent the undesirable scaling relations by optimizing the adsorption configurations of reaction intermediates with the synergistic effects of Mo and Ni on the Ni_3Mo surface. As a result, Ni_3Mo exhibits excellent NRR activity with an ultralow limiting potential (U_L) value of -0.19 V vs. reversible hydrogen electrode (RHE), which is better than HER activity. Meanwhile, the active centers for NRR on the Ni_3Mo surface are greatly protected from competitive H adsorption, ruling out the detrimental effect of competitive adsorption of H and N_2 . Therefore, the intermetallic Ni_3Mo with great activity and selectivity could be an optimal electrocatalyst to achieve qualified catalytic performance for NRR.

2. Experimental section

2.1. Calculation methods

All the spin-polarized density functional theory (DFT) calculations were performed by the Vienna ab initio simulation package (VASP) with the projected augmented wave (PAW) method [26–29]. The generalized gradient approximation (GGA) with Perdew-Burke-Ernzerhof exchange-correlation functional (PBE) was utilized for describing the electronic interactions [30]. The cut off energy was set to 450 eV for our DFT calculations. The empirical correction in Grimme's scheme (DFT-D3) was employed to describe the van der Waals interactions [31]. During the geometrical optimization, the energy and force convergence criteria were set to 1.0×10^{-5} eV and 0.02 eV/Å, respectively. The $\text{Ni}_3\text{Mo}(211)$ surface model was constructed by 2×2 repeated unit cells. The structure model of Ni_3Mo is composed of six atomic layers, where the upper two layers are fully relaxed while the bottom layers are constrained. The Brillouin zone was sampled using the Monkhorst-Pack mesh with a k -point grid of $3 \times 3 \times 1$. To avoid the interactions between two periodic images, a vacuum distance of 15 Å was adopted in the z direction. Note that the energy change of solvation-induced stabilization of reaction intermediates in the NRR is within 0.2 eV while only affecting the limiting potential value for NRR by ~ 0.1 V, the effects of solvation were not taken into account due to the high computational cost [32,33]. The ab initio molecular dynamics (AIMD) simulations within the NVT ensemble were employed to evaluate the N_2 adsorption on the $\text{Ni}_3\text{Mo}(211)$ surface at 300 K under aqueous conditions, in which the simulation time was set to 10 ps with a time step of 1 fs. The LOBSTER code (3.1.0) was used for calculating the crystal orbital Hamiltonian population (COHP) of the $\text{N}\equiv\text{N}$ bond [34]. For all the slab models, the possible oxide situation is not considered since it could be easily

removed during the activation process of electrochemical measurement. The adsorption energies (ΔE_{*x}) are defined by,

$$\Delta E_{*x} = (E_{*x} - E_x - E^*) \quad (1)$$

where the E_{*x} , E_x , and E^* are the total energy of the adsorption system, the chemical potential of adsorbate, and the energy of the catalyst, respectively. The changes of Gibbs free energy (ΔG) of elementary steps were calculated based on the computational hydrogen electrode model with using one-half of the chemical potential of H_2 as the chemical potential of the proton-electron pair [16,35]. The ΔG could be calculated by,

$$\Delta G = \Delta E + \Delta E_{\text{ZPE}} - T\Delta S \quad (2)$$

where the ΔE , ΔE_{ZPE} , ΔS and T denote the reaction energy, the zero-point energy, the entropy difference, and the reaction temperature (298.15 K), respectively. The entropy terms of the gas molecules (N_2 , H_2 and NH_3) were obtained from the standard values of thermodynamics [36].

The U_L is considered a reasonable descriptor for estimating the intrinsic NRR activity of electrocatalysts, which is the minimum applied potential required to ensure that all the electron-transfer steps can be downhill to favor the production of NH_3 . The U_L can be calculated by,

$$U_L = -\Delta G_{\text{max}}/e \quad (3)$$

where the ΔG_{max} represents the most positive free energy change of elementary steps during the NRR process. The e denotes the electron transferred during the elementary reaction.

2.2. Chemicals

Molybdenum wire (Mo, 99.95%), nickel sheet (Ni, 99.5%), sodium hydroxide (NaOH, 96.0%), salicylic acid ($\text{C}_7\text{H}_6\text{O}_3$, 99.5%), sodium sulfate (Na_2SO_4 , 99.0%), ammonium chloride (NH_4Cl , 99.5%) were purchased from Sinopharm Chemical Reagent Co., China. P-dimethylaminobenzaldehyde (PDAB, $\text{C}_9\text{H}_{11}\text{NO}$, 99%) was obtained from Aladdin Chemistry Co., Ltd. (Shanghai, China). Sodium hypochlorite solution (NaClO, available Cl 4.0%) was purchased from Shanghai Macklin Biochemical Co., Ltd. Hydrochloric acid (HCl, 35.0–38.0%), hydrogen peroxide (H_2O_2 , 30%), and ethanol ($\text{C}_2\text{H}_5\text{OH}$, 99.7%) were obtained from Beijing Chemical Works, China. Hydrazine monohydrate ($\text{N}_2\text{H}_4 \cdot \text{H}_2\text{O}$, 80.0%) was obtained from Adamas-beta Chemical Co. Nitrogen (N_2 , high purity 99.999%) and argon (Ar, high purity 99.999%) were purchased from Ju'yang gas Co., China. The ultrapure water with a resistivity of 18.2 MΩ cm was used in all experiments. All of the chemicals were used without further purification.

2.3. Synthesis of Ni_3Mo

The Ni_3Mo alloy was prepared by arc melting method with alloying pure Ni and Mo for about 3:1 in a Ti-gettered high-purity argon atmosphere. These ingots were re-melted 5 times and then annealed at 900 °C for 12 h under an argon gas atmosphere to effect homogenization of the composition. The result alloy ingots were cut with a diamond saw into thin sheets with a thickness of ~ 400 μm, washed with ethanol and ultrapure water several times to remove chemical residues and used for electrochemical measurements and microstructure characterizations.

2.4. Structural characterizations

Field-emission scanning electron microscope (JSM-7900 F, JEOL, 15 kV) equipped with X-ray energy-dispersive spectroscopy (EDS) was performed to investigate the morphology and chemical composition of intermetallic Ni_3Mo . X-ray diffraction (XRD) data and high-resolution transmission electron microscopy (HRTEM) image of Ni_3Mo were obtained from the smartlab (9kw) X-ray diffractometer with a

monochromated Cu K α radiation and the field-emission transition electron microscope (JEM-2100 F, JEOL), respectively. The X-ray photoelectron spectroscopy (XPS) was utilized to investigate the surface charge distribution of Ni₃Mo via the Thermo ECSALAB 250. The charging effects were compensated by shifting binding energies according to the C 1 s peak (284.8 eV). The absorbance data of the spectrophotometer were measured on an ultraviolet-visible spectrophotometer (UV-2600i).

2.5. Electrochemical NRR measurements

The high concentration of protons in acid solution improves competitive H adsorption and boosts the HER, whereas the low concentration of protons in alkaline solution restricts proton transfer to NRR on active sites and thus hinder the protonation of N₂ [37,38]. As a result, the neutral pH electrolyte was employed to limit the local concentration of protons around the active sites of Ni₃Mo for a better NRR performance. Before the NRR test, the Nafion membrane was pretreated in solutions of 5 wt% H₂O₂, 0.5 M H₂SO₄ and ultrapure water with boiling at 80 °C for 1 h, respectively. An Ivium-n-Stat electrochemical workstation was used to conduct the electrochemical measurements of NRR. A platinum plate and Ag/AgCl (saturated KCl electrolyte) served as counter electrode and electrode, respectively. The as-synthesized bulk Ni₃Mo catalyst was cut into 2 × 5 mm² and worked as working electrode. All electrochemical measurements were completed in a sealed H-type cell separated by the Nafion membrane. The corresponding potentials in this work were converted to the RHE as the following equation,

$$E(\text{vs-RHE}) = E(\text{vs-Ag/AgCl}) + 0.197 \text{ V} + 0.0591 \times \text{pH} \quad (4)$$

The electrochemical NRR process of catalyst was conducted in N₂-saturated 0.1 M Na₂SO₄ solution for 2 h. The working electrode was activated in Ar-saturated electrolyte by cycle voltammetry (CV) to remove the surface impurities before the NRR testing. Subsequently, the nitrogen (99.999%) was continuously fed into the cell during the NRR electrolysis [39,40]. The production of NH₃ has been detected with an ultraviolet-visible (UV-vis) spectrophotometer by salicylic acid analysis method after the NRR test of 2 h.

2.6. Determination of ammonia

The concentration of NH₃ in 0.1 M Na₂SO₄ solution was quantified by UV-vis spectrophotometry using the salicylic acid analysis method [41]. Firstly, 4 mL aliquot of the electrolyte solution was pipetted from the cathode cell. Then 50 μ L of oxidizing solution composed of 0.05 M NaClO and 0.75 M NaOH aqueous solution, 500 μ L of coloring solution containing 0.4 M C₇H₆O₃ and 0.32 M NaOH and 50 μ L of catalyst solution that prepared by diluting 0.1 g of Na₂[Fe(CN)₅NO]·2 H₂O to 10 mL with deionized water were added into above electrolyte solution in turn. After two hours in dark, the absorption spectra of the resulting solution were measured at a wavelength at $\lambda = 659.8$ nm. The concentration-absorbance calibration curves were built using standard NH₄Cl solution with NH₃ concentrations from 0 to 1.0 μ g mL⁻¹ in 0.1 M Na₂SO₄ solution.

2.7. Determination of hydrazine hydrate

The concentration of hydrazine hydrate (N₂H₄) was determined by the Watt and Chrisp method [42]. The color-developing agent was the miscible liquids of Para-(dimethylamino) benzaldehyde (5.99 g), HCl (12 M, 30 mL) and ethanol (300 mL). 2 mL electrolyte was mixed with 2 mL of the chromogenic reagent added and under the dark for 30 min. A linear fit was generated from the standard measurements and used to calculate the concentrations of N₂H₄ at the absorbance at $\lambda = 456$ nm.

2.8. Calculation of NH₃ yield and Faradaic efficiency (FE)

The yield rate of NH₃ during the NRR process was obtained by,

$$\text{Yield rate} = \frac{C \times V}{t \times A} \quad (5)$$

where the C, V, t, and A represent the concentration of NH₃ (μ g mL⁻¹) in the electrolyte, the volume of the cathodic chamber (mL), the time for electrocatalysis (2 h in this work) and the geometric area of the Ni₃Mo (cm²), respectively. Besides, the FE was calculated via the following equation,

$$\text{FE} = \frac{3 \times F \times C \times V}{17 \times Q} \quad (6)$$

where the F and Q represent the faraday constant (96485 C mol⁻¹) and the total electricity consumption during the NRR process, respectively.

3. Results and discussion

3.1. Scaling relations analysis

Efficient screening descriptors are desired for roughly evaluating the NRR activity of electrocatalysts since NRR is a complicated process. The active sites with relatively strong N₂ adsorption capacity are essential to improve the local concentration of N₂ around and activate the N \equiv N bond for further hydrogenation [43]. Furthermore, the adsorption strengths of NH_z intermediates are linearly correlated with the ΔE^*_{N} due to the scaling relations, which could be used to roughly evaluate the destabilization of the NH_z species [2,44,45]. Thus, the $\Delta E^*_{\text{N}_2}$ and ΔE^*_{N} of various systems [including the Ni(111), Mo doped Ni(111), Ni₄Mo, Ni₃Mo, Ni doped Mo(110) and Mo(110) surfaces] were calculated to obtain an optimal electrocatalyst with high N₂ affinity and smooth hydrogenation of NH_z species. The N species could be adsorbed on T_{Mo} and B_{MoNi} sites of Ni₃Mo surface with the ΔE^*_{N} of -0.84 and -1.03 eV, respectively (Fig. S1), implying that the B_{MoNi} site could be preferentially occupied by N species. Thus, the value of ΔE^*_{N} on the B_{MoNi} site was used as a presentation to evaluate the destabilization of the NH_z species. Except for the Ni₃Mo, the $\Delta E^*_{\text{N}_2}$ and ΔE^*_{N} values of systems follow the same trend (the higher the N₂ affinity, the stronger the N adsorption), denoting that their NRR activities are restricted by the scaling relations (Fig. 1a). Remarkably, the Ni₃Mo circumvents the undesirable scaling relations and achieves selective stabilization of the reaction intermediates during the NRR process, as evidenced by its high N₂ affinity but a weaker N adsorption strength. Hence, Ni₃Mo is chosen as a promising candidate for further investigations.

3.2. Geometric and electronic structure

The intermetallic Ni₃Mo has an orthorhombic D0a crystal structure within the *Pmmn* space group [46]. Based on the experimental characterization of previous literature and our experimental evidence, the (211) surface as the mainly exposed surface of bulk Ni₃Mo was chosen for evaluating the NRR performance [47]. The geometric structures of the Ni₃Mo (211) surface are shown in Fig. 1b. Both Mo and Ni atoms are exposed on the surface, and Mo is mainly coordinated to Ni with a bond length of 2.50 Å. The distances between surface Mo atoms are 3.68 and 4.32 Å, respectively. The Bader charge population analysis shows that the surface Mo atom of Ni₃Mo has a positive charge of +0.57 e, whereas the adjacent Ni atoms have negative charges of -0.23 and -0.18 e, respectively, indicating the electron transferring from Mo to Ni (Fig. 1c). The partial density of states (PDOS) of Mo and Ni atoms on the Ni₃Mo (211) surface were also calculated (Fig. 1d). Owing to the electron transfer between Ni and Mo species, the PDOS of the Ni-3d orbitals on the Ni₃Mo(211) surface are mainly located below the Fermi level (*E_f*) while that of Mo-4d orbitals are localized above the *E_f*, suggesting that

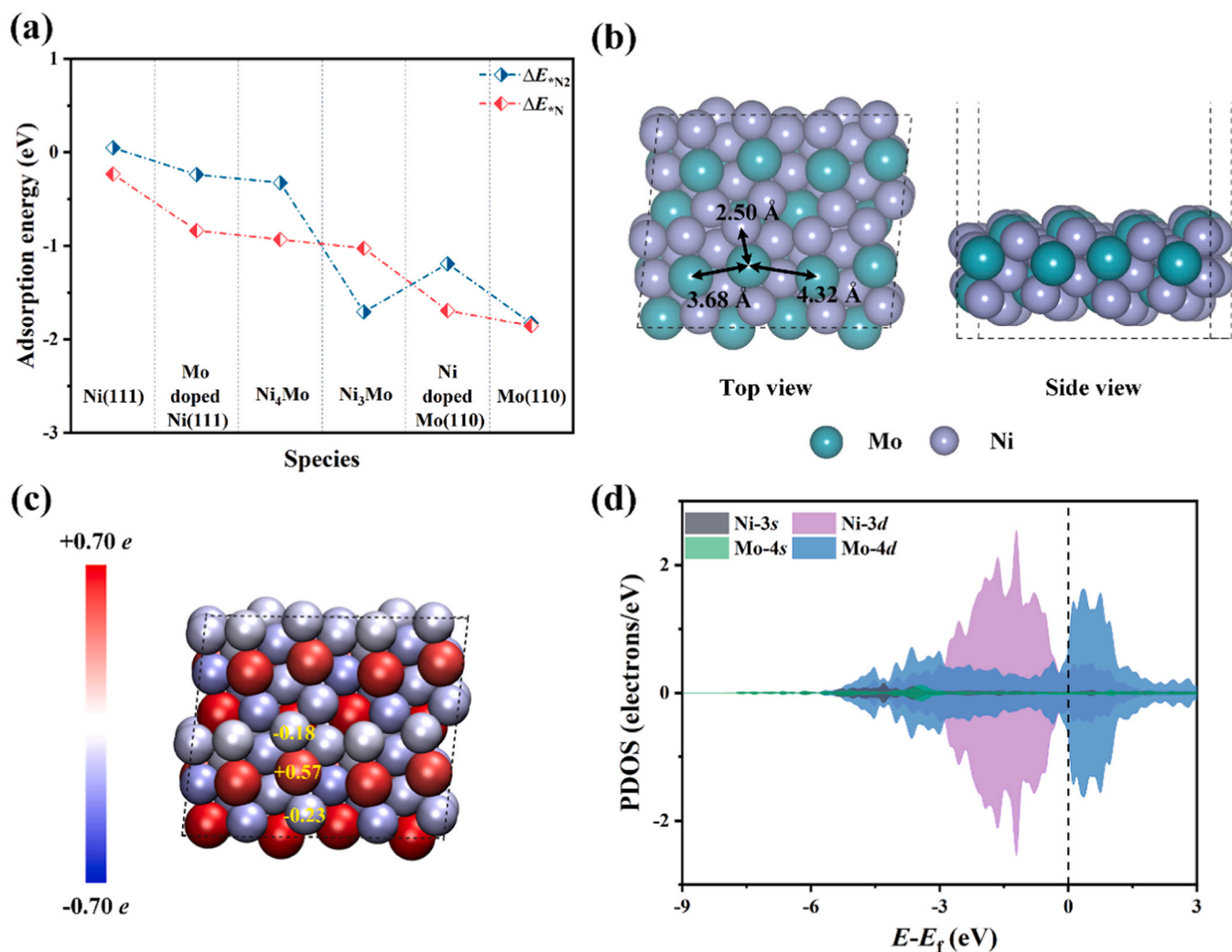


Fig. 1. (a) The ΔE_{N_2} and ΔE_N values of various systems, including the Ni(111), Mo doped Ni(111), Ni₄Mo, Ni₃Mo, Ni doped Mo(110) and Mo(110) surfaces. (b) Geometric structure of the Ni₃Mo(211) surface. The aquamarine blue and purple balls represent Mo and Ni atoms, respectively. (c) Bader charge population analysis on Ni₃Mo(211) surface. The positive (negative) charge indicates the electron loss (gain). (d) The PDOS of Ni and Mo atoms on the Ni₃Mo(211) surface, respectively.

surface Mo atoms possess more empty orbitals for bonding with N₂ molecule via the "σ-acceptance" process [48].

3.3. Adsorption and activation of nitrogen

Both the adsorption of N₂ and the activation of the N≡N bond are essential for NRR, where the former is the initial step of NRR while the latter is generally regarded as the key for the subsequent hydrogenation process. There are various N₂ adsorption sites on the Ni₃Mo(211) surface, including the top site of the Mo atom (T_{Mo} site), the bridging site between Mo and Ni atoms (B_{MoNi} site) as well as the bridging sites consisting of two adjacent Mo atoms (B_{1MoMo} and B_{2MoMo} sites) with distances of 3.68 and 4.32 Å, respectively. The adsorption configurations and corresponding ΔE_{N_2} values are shown in Fig. 2a. Both B_{1MoMo} (-1.71 eV) and B_{2MoMo} (-1.65 eV) sites exhibit stronger adsorption capacity than other sites (-1.08 and -1.00 eV on T_{Mo} and B_{MoNi} sites, respectively). Moreover, the N≡N bond lengths of T_{Mo}, B_{MoNi}, B_{1MoMo} and B_{2MoMo} sites have been elongated from 1.115 Å in the gas phase to 1.138, 1.188, 1.244 and 1.235 Å, respectively, suggesting the effective activation of N₂ on B_{1MoMo} and B_{2MoMo} sites. Additionally, the adsorption strengths of B_{1MoMo} and B_{2MoMo} sites are comparable to the sites on the hollow sites of pristine Mo(110) surface with the $\Delta E_{N_2} = -1.83$ eV (Fig. S2), indicating that the neighboring Ni atoms with poor N₂ adsorption have a little detrimental effect on the inherent N₂ affinity of

Mo sites. Furthermore, the COHP analysis and the corresponding integral values (ICOHP) of the N≡N bond were investigated to evaluate the activation degree of N₂ adsorbed on various active sites (a more negative value of ICOHP represents a lower activation of the N≡N bond). As illustrated in Fig. S3, the ICOHP values of the N≡N bond followed the order: free N₂ (-11.66) < T_{Mo} (-9.42) < B_{MoNi} (-8.04) < B_{2MoMo} (-6.67) < B_{1MoMo} (-6.59), demonstrating that both the B_{1MoMo} and B_{2MoMo} sites exhibit effective activation on N₂ molecule. The more negative ICOHP value of the B_{2MoMo} site can be attributed to the slightly longer Mo-N bond (1.93 Å for B_{2MoMo} while 1.90 Å for B_{1MoMo}), which weakens the interaction between Mo and N atoms. Consequently, the B_{1MoMo} and B_{2MoMo} sites are regarded as the main active sites of Ni₃Mo for NRR and will be studied further in the following discussion.

For simplicity, we took the B_{1MoMo} site as a representative to elucidate the activation mechanism of N₂ because of its most negative ΔE_{N_2} value. The PDOS of the B_{1MoMo} site before and after the N₂ adsorption were plotted in Fig. 2b. For the free N₂ molecule, the N≡N bond is composed of three molecule orbitals (one σ and two π), in which the N-2p_x orbitals construct the σ orbital of the N≡N bond while the N-2p_y and -2p_z orbitals construct the π and π* orbitals. Obviously, strong hybridizations between the Mo-4d_{z2}, Mo-4d_{x2-y2}, and the bonding N₂-σ orbitals are found around -6 eV after N₂ adsorption, suggesting that Mo accepts the σ-electrons of N₂ molecule through Mo-4d_{z2} and -4d_{x2-y2} orbitals, favoring the formation of Mo-N bond. Meanwhile, the bond

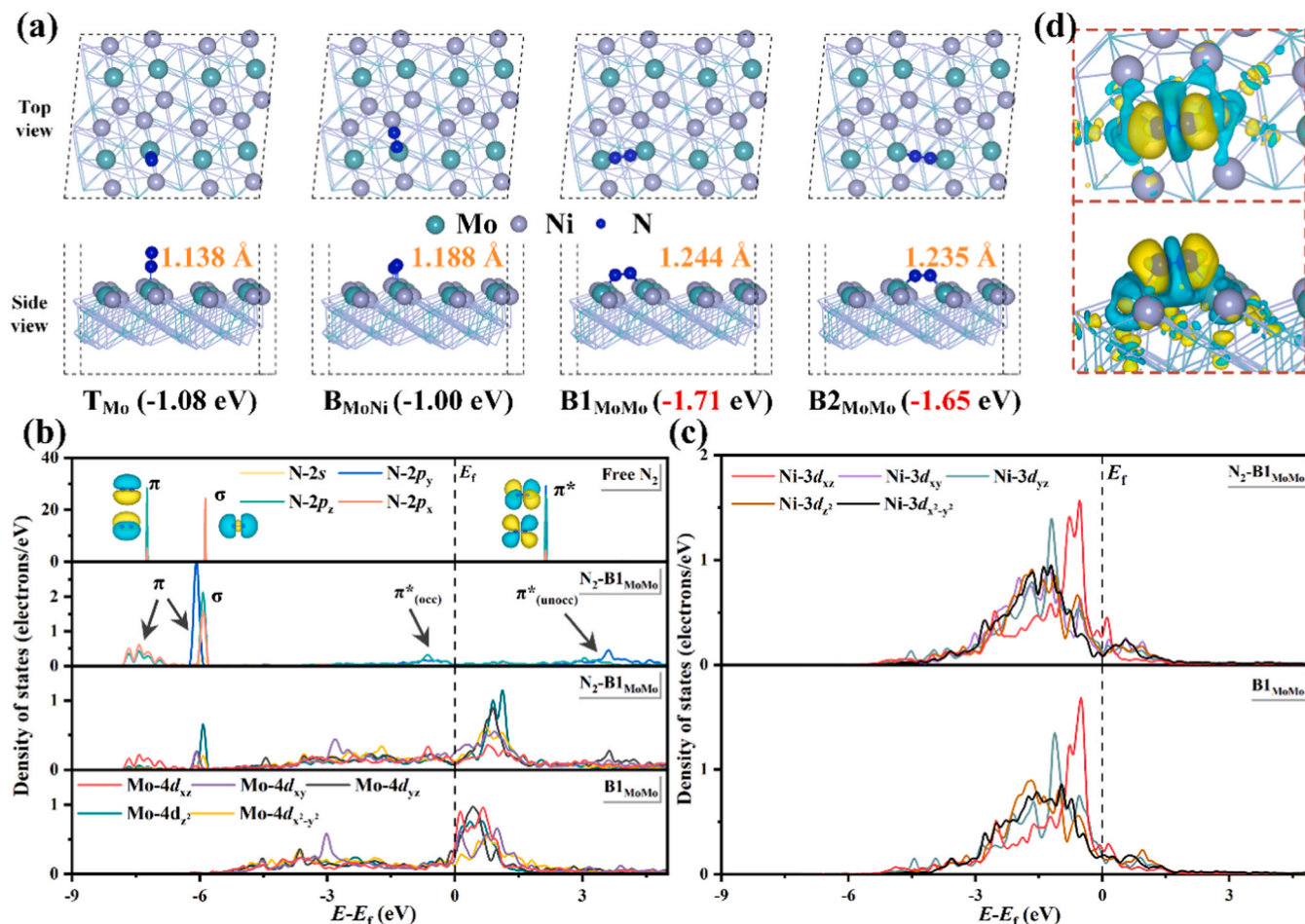


Fig. 2. (a) The adsorption energy value of N_2 species at various adsorption sites on $\text{Ni}_3\text{Mo}(211)$ surface. (b) The PDOS of N-2s and 2p orbitals (N-2p_x, -2p_y and -2p_z) of free N_2 molecule and N_2 adsorbed at the B1_{MoMo} site ($\text{N}_2\text{-B1}_{\text{MoMo}}$) and Mo-4d orbitals (Mo-4d_{xz}, -4d_{xy}, -4d_{yz} and -4d_{x²-y²} orbitals) of the B1_{MoMo} and the $\text{N}_2\text{-B1}_{\text{MoMo}}$. (c) The PDOS of Ni-3d orbitals (Ni-3d_{xz}, -3d_{xy}, -3d_{yz}, -3d_{z²} and -3d_{x²-y²} orbitals) of the Ni atoms neighboring B1_{MoMo} site before and after N_2 adsorption. (d) The electron density difference of N_2 adsorbed on the B1_{MoMo} site, where yellow and blue isosurfaces indicate electron density accumulation and depletion, respectively.

order of the $\text{N}\equiv\text{N}$ bond reduces as the number of electrons in the bonding σ orbitals of N_2 decreases [9]. Additionally, all of the Mo-4d orbitals are hybridized with the antibonding $\text{N}_2\text{-}\pi^*$ orbitals, leading to the $\text{N}_2\text{-}\pi^*$ orbitals being broadened and partially occupied [denoted as π^*_{occ} and π^*_{unocc}] by the electrons from Mo-4d orbitals. Among the Mo-4d orbitals, notable hybridizations between the Mo-4d_{xz}, Mo-4d_{xy}, Mo-4d_{yz} and $\text{N}_2\text{-}\pi^*$ orbitals are observed, showing that the d-electrons transfer to the $\text{N}_2\text{-}\pi^*$ orbitals mainly through the Mo-4d_{xz}, -4d_{xy} and -4d_{yz} orbitals for the " π -donation" process, efficiently weakening the inert $\text{N}\equiv\text{N}$ bond. The PDOS of the neighboring Ni atoms were also calculated. As illustrated in Fig. 2c, the Ni-3d_{xz} orbital appears empty orbitals above the E_f after N_2 adsorption, indicating that the electrons of Ni are transferred to neighboring Mo atoms during N_2 adsorption, indirectly enhancing the injection of electrons from Mo into N_2 for activation. Furthermore, the Bader charge analysis results suggest that the average value of Ni atoms around the B1_{MoMo} site changes from -0.21 to -0.16 e, signifying the electronic redistribution of Ni. The above electron transfer process can be observed by the diagram of charge density difference, where electron accumulation is present on the anti-bonding orbitals of N_2 and electron depletion is found on the Mo atoms and the bonding orbitals of N_2 (Fig. 2d).

3.4. Electrochemical reduction of nitrogen

Since the N_2 molecule is adsorbed on the $\text{Ni}_3\text{Mo}(211)$ surface with a

side-on configuration (both the N atoms bonding with Mo), the hydrogenation processes can occur via three pathways: enzymatic, consecutive and mixed (Fig. 3a), in which six elemental proton-coupled electron transfer steps are involved. For the enzymatic pathway, hydrogenation processes occur alternately on the two N atoms, while for the consecutive pathway, hydrogenation processes occur preferentially on the one N atom to generate the first NH_3 molecule. The hydrogenation processes in the mixed pathway initially follow the enzymatic pathway until *NHNH_2 is produced, then shuttle to the consecutive pathway. Herein, all possible routes on B1_{MoMo}, B2_{MoMo} and B_{MoNi} sites for NRR were investigated, and the corresponding reaction intermediates on each pathway are summarized.

For the B1_{MoMo} site, the *N_2 prefers to be protonated through the mixed pathway. As depicted in Fig. 3b, the protonation step of *N_2 to *NNH ($\text{*N}_2 + \text{H}^+ + e^- \rightarrow \text{*NNH}$) is exothermic with the ΔG of -0.06 eV, implying the great activation of $\text{N}\equiv\text{N}$ bond. The proton/electron pairs (H^+/e^-) attack alternatively the two N atoms to form *NHNH and *NHNH_2 with uphill ΔG of 0.16 and 0.32 eV, respectively. Then, the H^+/e^- attacks the *NH_2 part of *NHNH_2 to form *NH species and release the first NH_3 molecule ($\text{*NHNH}_2 + \text{H}^+ + e^- \rightarrow \text{*NH} + \text{NH}_3$). The corresponding ΔG value is -1.00 eV. In the following steps, the protonation of *NH can proceed via $\text{*NH} \rightarrow \text{*NH}_2 \rightarrow \text{*NH}_3$ with the ΔG of -0.30 and 0.13 eV, respectively. As a result, the potential limiting step (PLS) for NRR is the formation of *NHNH_2 ($\text{*NHNH} + \text{H}^+ + e^- \rightarrow \text{*NHNH}_2$) due to its maximum ΔG value. Thus, the U_L for the mixed pathway is -0.32 V

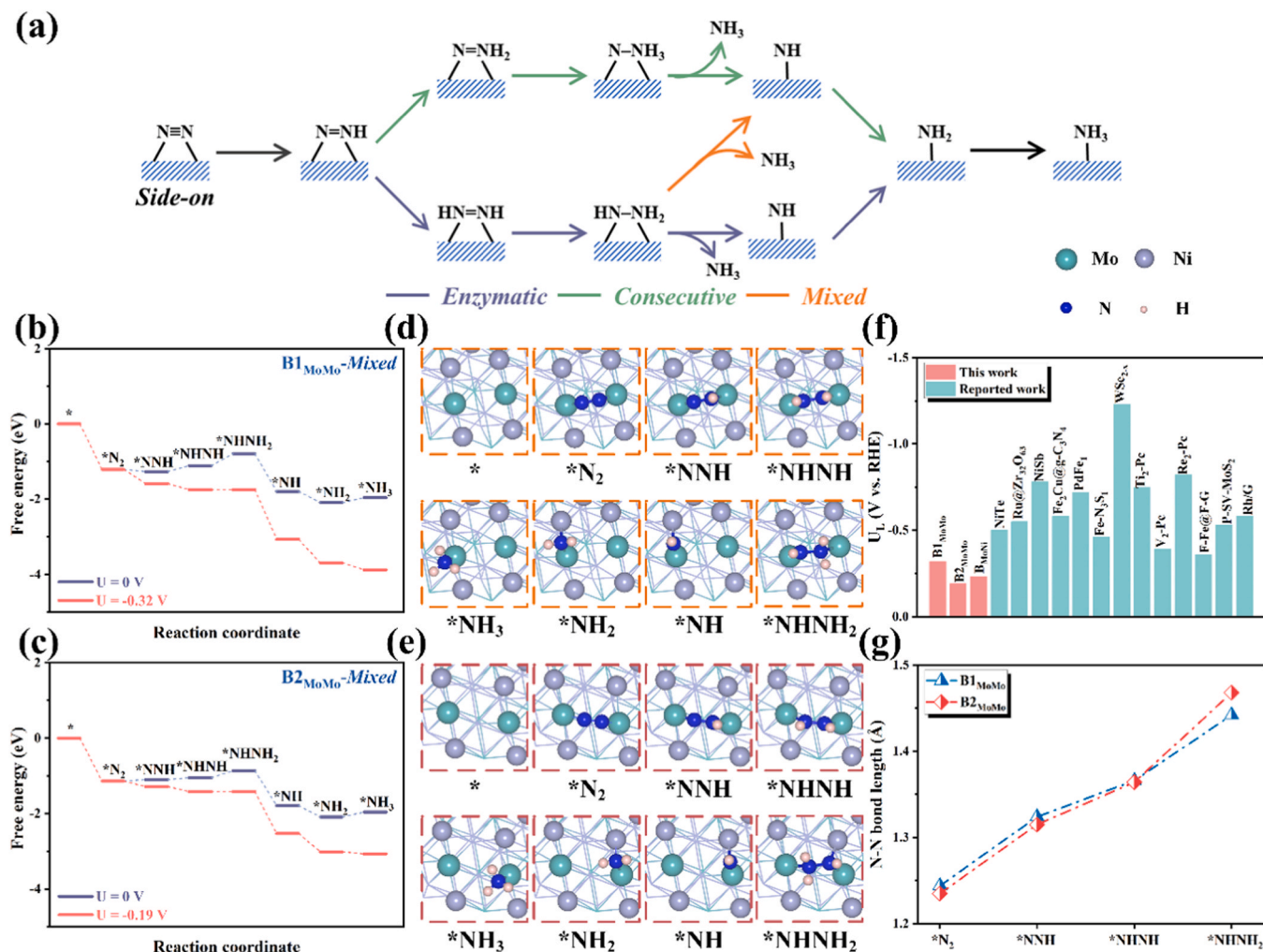


Fig. 3. (a) Schematic illustration of the possible reaction mechanisms during the N₂ reduction through side-on adsorption pattern. The minimum Gibbs free energy change diagrams of (b) B1_{MoMo} and (c) B2_{MoMo} sites of Ni₃Mo(211) surface for NRR. The corresponding configurations of intermediates of the (d) B1_{MoMo} and (e) B2_{MoMo} sites, respectively. The Mo, Ni, N and H are shown as aquamarine blue, purple, blue and pink balls, respectively. (f) Comparison of U_L for NRR on Ni₃Mo(211) surface and other reported NRR electrocatalysts. (g) The N-N bond length changes at the B1_{MoMo} and B2_{MoMo} sites during the NRR process.

vs. RHE. Besides, the free energy diagrams and corresponding reaction intermediates of enzymatic and consecutive pathways are also shown in Fig. S4, in which the corresponding U_L values are -0.32 and -0.40 V vs. RHE, respectively.

The mixed pathway is also a minimum free energy path for the NRR on the B2_{MoMo} site. As shown in Fig. 3c, *NNH is formed with a slightly uphill ΔG of 0.04 eV, which is consistent with our above COHP analysis of the N≡N bond. Compared with the B1_{MoMo} site, the following two protonation steps to form *NHNH and *NHNH₂ species are more feasible, with smaller ΔG values of 0.05 and 0.19 eV, respectively. In the following step, the N-N bond in the subsequent step is broken to form *NH species and release the first NH₃ molecule, the process of which is exothermic with $\Delta G = -0.93$ eV. The protonation of *NH to *NH₂ is spontaneous ($\Delta G = -0.30$ eV) while the formation of *NH₃ is slightly uphill (0.13 eV). Therefore, the PLS for the mixed pathway on the B2_{MoMo} site is the protonation of *NHNH into *NHNH₂. The corresponding U_L is as low as -0.19 V vs. RHE, indicating excellent catalytic activity for NRR. In addition, the corresponding U_L values of the enzymatic and consecutive pathways are -0.24 and -0.33 V vs. RHE, respectively. The corresponding free energy diagrams and reaction intermediates were given in Fig. S5.

For the B_{MoNi} site, the minimum free energy path for the NRR is the mixed pathway (Fig. S6). The first hydrogenation step of *N₂ to *NNH is more energetically unfavorable ($\Delta G = 0.23$ eV) than that of the B1_{MoMo}

and B2_{MoMo} sites, which is an endothermic process. Then, the *NNH is spontaneously hydrogenated to *NHNH and *NHNH₂ with the corresponding ΔG values of -0.13 and -0.37 eV, respectively. Subsequently, the protonation of *NHNH₂ produces an NH₃ molecule and form *NH species with a negative ΔG (-0.96 eV), which is exothermic. The remaining *NH proceeds the protonation to form *NH₂ and *NH₃ species, where the corresponding ΔG values are -0.30 and 0.13 eV, respectively. Therefore, for the B_{MoNi} site, the PLS for the NRR along the mixed pathway is the first protonation step of *N₂ species with the U_L of -0.23 V vs. RHE, indicating the insufficient activation of N₂ but a great destabilization of *NH₂ species. Additionally, the free energy diagrams of the NRR on the B_{MoNi} site along the enzymatic and consecutive pathways are illustrated in Fig. S7. The corresponding U_L values are -0.44 and -0.23 V vs. RHE, respectively. Thus, the active sites of Ni₃Mo exhibit excellent NRR activity. Notably, when the N₂ molecule firstly adsorbed on the B2_{MoMo} site, the Ni₃Mo could subtly combine the advantage of B2_{MoMo} (N₂ activation) and B_{MoNi} (*NH₂ destabilization) sites, which effectively decrease the energy barrier during the NRR process.

The outstanding NRR activity of B1_{MoMo} and B2_{MoMo} sites should be attributed to the synergistic effect of Ni and Mo, which optimizes the adsorption configurations of reaction intermediates during the NRR process. The corresponding configurations of intermediates on the B1_{MoMo} and B2_{MoMo} sites are shown in Figs. 3d and 3e. The N₂ molecule

could be firstly adsorbed on the B1_{MoMo} and B2_{MoMo} sites and effectively activated for further hydrogenation. As the protonation steps proceed, the N-N bond is gradually elongated until the hydrogenation of *NHNH₂, at which point the N-N bond is cleaved. Meanwhile, the produced *NH species is adsorbed by the B_{MoNi} site for the subsequent protonation steps with relatively low ΔG values. The ΔG values of hydrogenation process of *NH_z (z = 1 or 2) on the Mo(110) surface was calculated for investigating the role of Ni species. The protonation processes of *NH ($\Delta G = 0.51$ eV) and *NH₂ ($\Delta G = 0.35$ eV) on the Mo(110) are both endothermic because of the too strong adsorption toward N species. However, the corresponding processes appear on the Ni₃Mo(211) are more thermodynamically favorable with the ΔG of -0.30 and 0.13 eV, respectively, showing that the poor N affinity of Ni optimizes the protonation steps of *NH_z species and thus promote the NRR process on the Ni₃Mo surface. Therefore, the active sites for NRR on the Ni₃Mo surface are separated to realize the effective activation of the N≡N bond and destabilization of the NH_z intermediates simultaneously, cleverly bypassing the limitation of scaling relations. Additionally, under acid or alkaline conditions, the produced *NH₃ would be further protonated to form NH₄⁺ and thus released into the aqueous electrolyte, regenerating the catalytic active sites [49,50]. As shown in Fig. 3f, the U_L value of the B2_{MoMo} site on the Ni₃Mo surface is only -0.19 V while that of previously reported state-of-the-art catalysts are more negative than -0.36 V [6,14,22,32,51–57]. The smaller the absolute value of the

limiting potential, the higher the intrinsic catalytic activity of the active site. Theoretically, the NRR could be driven smoothly on the Ni₃Mo at -0.19 V, implying excellent intrinsic activity. Interestingly, although the Mo atoms of B1_{MoMo} and B2_{MoMo} sites are equivalent, B2_{MoMo} has a better NRR activity. To clarify it, the N-N bond lengths of corresponding intermediates at the B1_{MoMo} and B2_{MoMo} sites in the mixed pathway were investigated for the origin of the difference (Fig. 3g). The change of N-N bond length at the B2_{MoMo} site is larger than that at the B1_{MoMo} site during the *NNH → *NHNH → *NHNH₂ processes, demonstrating that the stress caused by the large distance between the two Mo atoms could promote the cleavage of N-N bond and thus decrease the corresponding ΔG .

3.5. Reaction selectivity toward NH₃ synthesis

In addition to the NRR activity, reaction selectivity is another important aspect of evaluating the catalytic performance. Generally, the H in protonic solvent would be easily adsorbed on most metal surfaces and block the active sites for NRR, dramatically limiting the initial step of NRR [6]. Therefore, the competitive adsorption of H and N₂ at the active sites on the Ni₃Mo(211) surface was studied. As depicted in Fig. S8, when the H is placed at the top site of Mo before structural optimization, the H would spontaneously move to the B_{MoNi} site, implying that H does not block the dominant adsorption sites of N₂

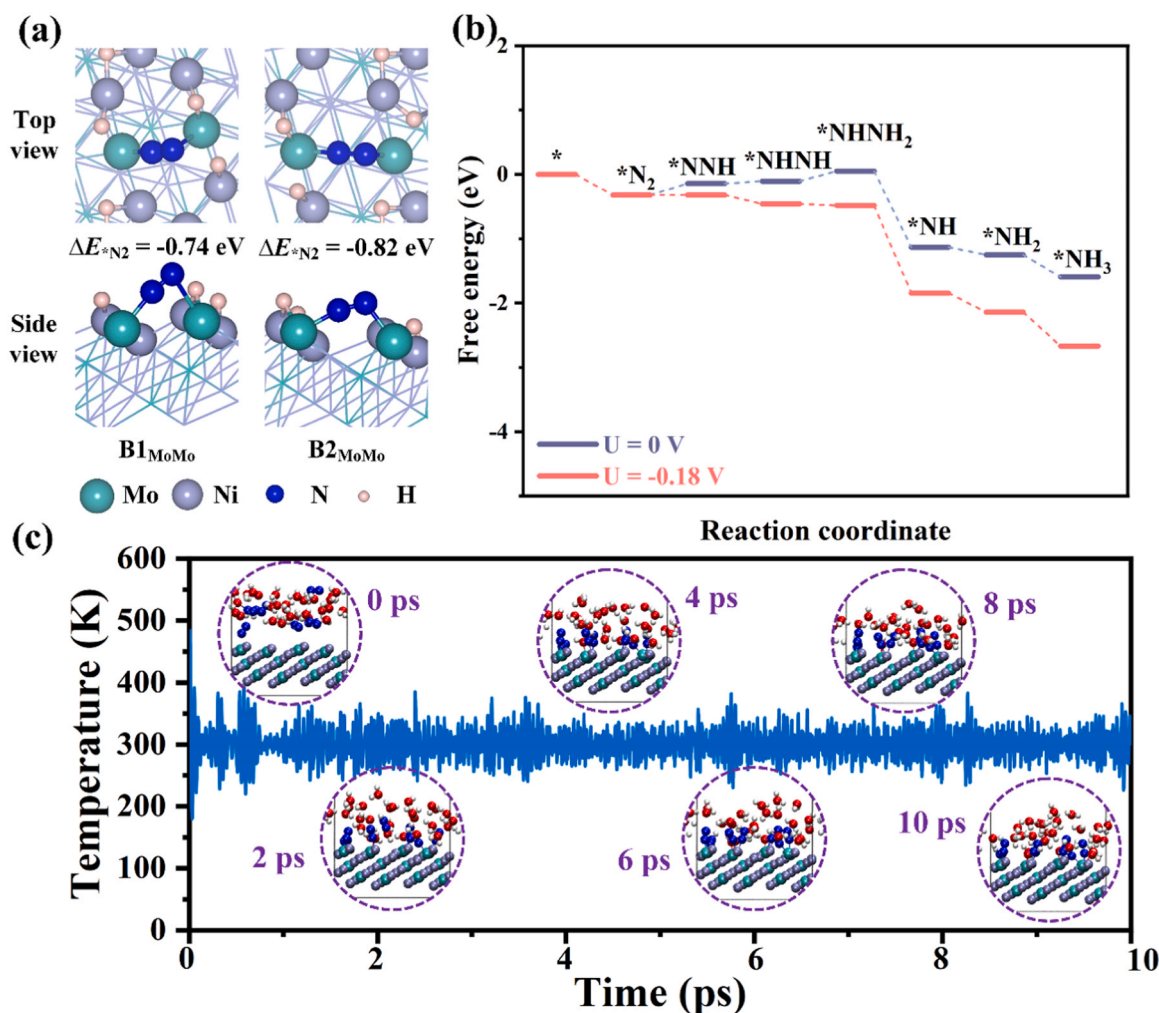


Fig. 4. (a) The adsorption configuration and the corresponding ΔE_{*N_2} for N₂ adsorbed at the B1_{MoMo} (left) and B2_{MoMo} (right) sites of the Ni₃Mo(211) surface with full H coverage. (b) Gibbs free energy diagram of the NRR on the B2_{MoMo} site of Ni₃Mo(211) surface with full H coverage. (c) The AIMD simulation of N₂ adsorbed on Ni₃Mo(211) surface at the temperature of 300 K under aqueous conditions. The insets are the corresponding atomic structures of the Ni₃Mo(211) surface at various time. The purple, turquoise, blue, red and white balls represent Ni, Mo, N, O and H, respectively.

(B1_{MoMo} and B2_{MoMo}). Besides, many NRR catalysts with high activity usually have better HER activity, which would harmfully decrease the selectivity toward NH₃. Thus, the HER activity of the Ni₃Mo(211) surface was calculated for evaluating the priority of NRR. The corresponding ΔG value of PLS for HER on the Ni₃Mo(211) surface is 0.49 eV, which is larger than that of NRR (Fig. S9), indicating that the initialization of the HER requires a more negative potential than the NRR. Evidently, the NRR is more probable to appear on the Ni₃Mo(211) surface than the HER, exhibiting a satisfactory selectivity toward NH₃.

In particular, the H adsorption process involves the transfer of protons and electrons, which could be facilitated with the negative electrode potential, while N₂ has been little affected [48,58]. The H species would inevitably cover the Ni₃Mo(211) surface when a high reduction potential is applied. Herein, the co-adsorption of H and N₂ was calculated. As shown in Fig. 4a, the N₂ still could effectively be adsorbed by the B1_{MoMo} and B2_{MoMo} sites of the Ni₃Mo(211) surface with full H coverage. The corresponding ΔE_{N_2} values are -0.74 and -0.82 eV, respectively, implying the absence of competitive adsorption between H and N₂ species on the Ni₃Mo(211) surface. Take the B2_{MoMo} site as an example to evaluate the corresponding NRR process (Fig. 4b and S10). The first hydrogenation of N₂ becomes the PLS of the NRR process since the H coverage weakens the ability for N₂ activation of surface Mo atoms. Moreover, the NRR activity of the B2_{MoMo} site with H coverage ($U_L = -0.18$ V vs. RHE) is slightly better than that without H coverage (-0.19 V vs. RHE), indicating that the intermetallic Ni₃Mo indeed exhibits good NRR activity in a protonic solvent. Besides, the adsorptions of OH[−] and H₂O on the Ni₃Mo(211) surface are also considered (Fig. S11). The corresponding adsorption energy values are -1.59 and -1.29 eV, which is more positive than that of N₂ on the B1_{MoMo} (-1.71 eV) and B2_{MoMo} (-1.65 eV), suggesting that the N₂ will be adsorbed advantageously. Furthermore, the AIMD simulations within

the NVT ensemble at a temperature of 300 K were performed to evaluate the N₂ adsorbed on the Ni₃Mo(211) surface under aqueous conditions. The snapshots of the Ni₃Mo(211) at 0, 2, 4, 6, 8 and 10 ps are given in Fig. 4c. Obviously, the N₂ molecules in solvent spontaneously move towards the surface and are preferentially adsorbed on the active sites within 2 ps. With time going by, the spontaneous hydrogenation of N₂ molecules can be observed, indicating that the N₂ would be effectively adsorbed and activated on the Ni₃Mo(211) surface under electrochemical conditions.

3.6. Proof-of-concept experiment

To confirm the above theoretical predictions, intermetallic Ni₃Mo was synthesized as an electrocatalyst for NRR. As illustrated by scanning electron microscopy-energy dispersive X-ray spectroscopy (SEM-EDS), the atomic ratio of Ni/Mo in the as-synthesized alloy sample is 75.5/24.5, which is consistent with the ratio of Ni₃Mo (Figs. S12a and b). The powder XRD of the as-synthesized sample is depicted in Fig. 5a, where the diffraction peaks located at 40.5°, 42.7°, 46.0°, 46.5°, 51.1°, 60.7°, 73.9° and 74.9° correspond to the (002), (020), (012), (211), (121), (221), (203) and (400) facets of intermetallic Ni₃Mo (PDF#17-0572) [59]. The above characterization results prove the successful preparation of intermetallic Ni₃Mo. Besides, the atomic structures were characterized by the HRTEM (Fig. 5b), where the (211) facet of Ni₃Mo is observed with the lattice spacings of 0.195 nm. Scanning transmission electron microscopy (STEM) and its elemental mapping under EDS indicate the high homogeneous dispersion of Ni and Mo species, implying the formation of a uniform alloy instead of the undesirable phase segregation (Figs. S12c, d and e). The XPS was employed to investigate the surface electronic structure of Ni₃Mo. As shown in Fig. S13, the Mo 3d spectrum of Ni₃Mo can be deconvoluted to three sets

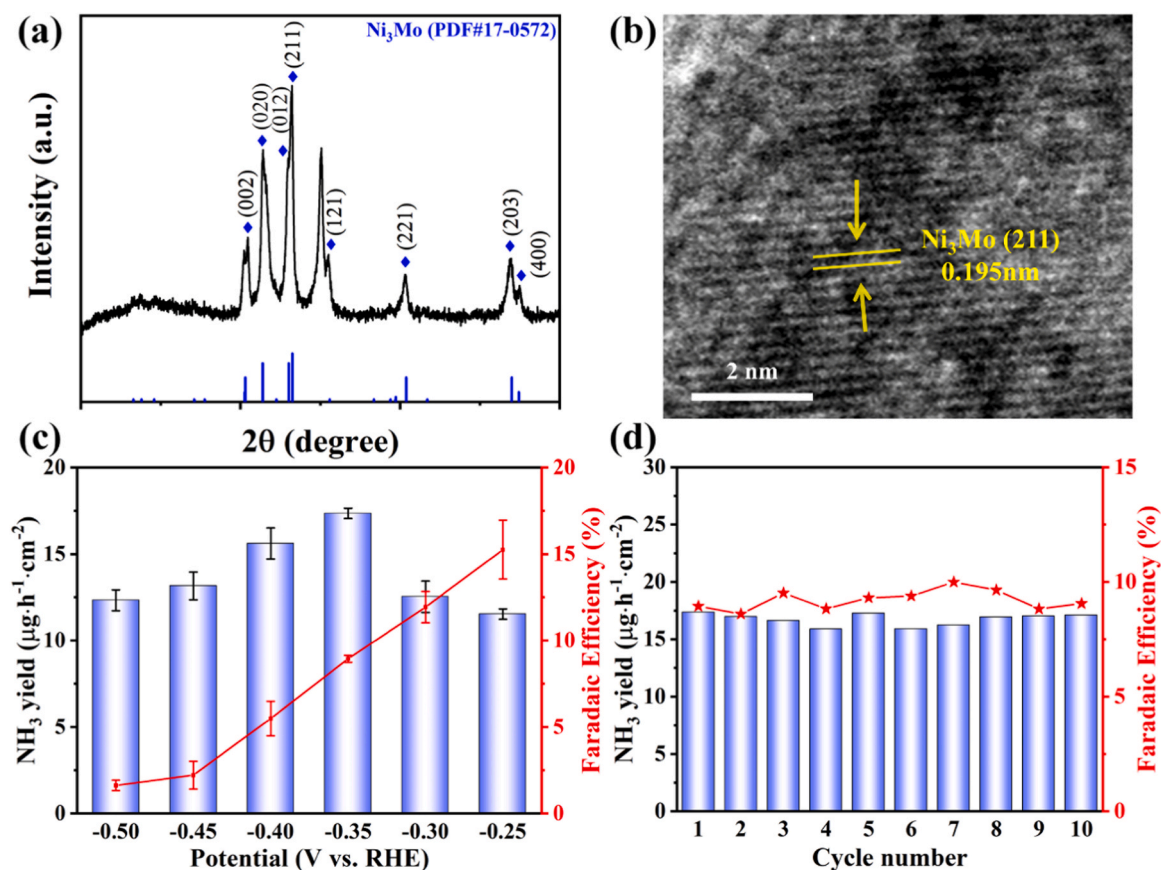


Fig. 5. (a) XRD pattern and (b) HRTEM images of Ni₃Mo sample. (c) NH₃ yield rates and FEs of Ni₃Mo under various potentials. (d) Durability of Ni₃Mo at the potential of -0.35 V vs. RHE under ambient conditions.

in doublets of Mo^0 , Mo^{4+} and Mo^{6+} with their $3d_{5/2}$ peaks centered at 227.3 eV, 228.5 eV and 232.1 eV, respectively, while Ni^0 and Ni^{2+} are located at 852.3 eV and 855.9 eV in Ni 2p spectrum [60–62]. The high oxidation states of Mo and Ni species are mainly because of the air exposure. Furthermore, the XPS of pure metal Mo and Ni counterparts were measured to investigate the charge distribution of surface atoms of Ni_3Mo . Clearly, the Mo-3d of synthesized Ni_3Mo shifts to higher binding energy while the Ni-2p shifts to lower binding energy, suggesting that the electrons of Mo transfer to Ni species, which is in line with our theoretical designs.

The electrochemical performance of Ni_3Mo was measured by a gas-tight two-compartment electrochemical cell in 0.1 M Na_2SO_4 electrolytes. As illustrated in Fig. S14a, the linear sweep voltammetry (LSV) curve of Ni_3Mo in N_2 -saturated electrolyte exhibits a large current density relative to that in Ar-saturated electrolyte, affirming the electrochemical responses for NRR. To estimate the NRR performance accurately, the Ni_3Mo was tested at different potentials with chronoamperometric measurements in N_2 -saturated electrolyte, where the generated NH_3 was quantified using the indophenol blue method (Fig. S14b). The corresponding NH_3 yield rates and FEs at various potentials were calculated based on the UV–vis absorption spectra of the electrolyte and the calibration curve of various NH_4^+ concentrations (Figs. S15 and S16). As shown in Fig. 5c, the Ni_3Mo catalyst exhibits superior catalytic activity with the highest NH_3 yield rate of $17.35 \pm 0.3 \mu\text{g h}^{-1} \text{cm}^{-2}$ at -0.35 V vs. RHE along with the FE of $8.94 \pm 0.2\%$. It should be noted that the intrinsic catalytic activity, the number of active sites, and the local concentration of N_2 around the active site, are the main factors of the FE towards NRR [63,64]. The greater these factors, the more likely the surface of the electrocatalyst will undergo NRR, resulting in a higher FE. The FE of Ni_3Mo for the NRR could be further optimized through surface modification (such as vacancy creation, heteroatom doping, nanocrystallization with nanoporosity and coating) for boosting N_2 transport in electrolyte and generating N_2 concentrating effect on the surface that greatly favors the NRR [43, 65–68].

Besides, to confirm N_2 adsorbed on the Ni_3Mo surface and reduced to NH_3 , the counterpart of the Ni_3Mo sample measured in the Ar-saturated electrolyte at -0.35 V vs. RHE is proceeded. As illustrated in Fig. S17, the UV–vis absorption spectrum of the counterpart is significantly lower than the catalyst tested in N_2 -saturated electrolyte, suggesting that the source of N in ammonia is the N_2 feeding gas. Moreover, no NH_3 is detected when conducting the chronoamperometric experiments at open-circuit potential using N_2 as the feeding gas, demonstrating that the detected NH_3 is generated via NRR rather than from contamination such as laboratory, equipment, and membrane [69]. Furthermore, the nuclear magnetic resonance (NMR) test was employed to accurately determine $\text{NH}_3/\text{NH}_4^+$. As depicted in Fig. S18, the NH_3 yield rate and FE_{NH_3} calculated by the NMR peak area and the calibration curve of $^{14}\text{NH}_4^+$ are close to the values obtained by UV–vis spectroscopy measurements, implying the accuracy of the measurement results from the UV–vis results. In addition, the selectivity of N_2 to NH_3 rather than other possible N-containing products was calculated. As shown in the Fig. S19, negligible by-product N_2H_4 was detected by the Watt and Chrisp method and the selectivity of N_2 to NH_3 is $\sim 95.55\%$ in liquid products at -0.35 V vs. RHE, suggesting that the Ni_3Mo has high selectivity for the electrocatalytic reduction of N_2 to NH_3 [42].

In addition to high NRR performance, the Ni_3Mo also exhibits great cycling stability. Both NH_3 yield rate and FE show only a slight change during ten times of consecutive recycling tests at -0.35 V vs. RHE (Fig. 5d). Additionally, by comparing the XRD pattern before and after electrocatalysis, Ni_3Mo catalyst shows a negligible change, implying the excellent structural stability (Fig. S20). To evaluate the comprehensive performance, the performance metrics of the as-synthesized Ni_3Mo and that of representative NRR reported previously were compared. As illustrated in Table S1, Ni_3Mo exhibits a better NH_3 yield rate and FE than that of recent literature data, which could be a promising

electrocatalyst for NH_3 synthesis.

4. Conclusions

In summary, we have theoretically investigated the Ni_3Mo inter-metallic compound as stable electrocatalysts for highly efficient and selective NRR using DFT calculations. The coordination between Mo and Ni constructs positively charged Mo atoms on the surface, achieving high N_2 affinity and efficient activation of the $\text{N}\equiv\text{N}$ bond. In particular, the scaling relations have been broken by the multiple active sites on the $\text{Ni}_3\text{Mo}(211)$ surface for achieving simultaneously activate N_2 and destabilize intermediates of NH_x species, resulting in splendid catalytic activity for NRR with the lowest U_L of -0.19 V vs. RHE. Furthermore, the adsorption sites for H and N_2 are separated on the $\text{Ni}_3\text{Mo}(211)$ surface, which eliminates the competitive adsorption on the active sites for better initiating the NRR. Meanwhile, the U_L value of HER on the $\text{Ni}_3\text{Mo}(211)$ surface is substantially greater than that of NRR, suggesting that NRR could arise preferentially on surface active sites. Our proof-of-concept experiment also confirms the above theoretical design, in which a high NH_3 yield rate of $17.35 \pm 0.3 \mu\text{g h}^{-1} \text{cm}^{-2}$ has been achieved at a low potential of -0.35 V vs. RHE. Thus, Ni_3Mo could be a promising electrocatalyst for NH_3 synthesis. Additionally, further improvements like as vacancy creation, heteroatom doping and coating could be employed to enhance NRR activity and selectivity.

CRedit authorship contribution statement

H. Y. Zhou: Conceptualization, Investigation, Writing – original draft. **Y. B. Qu:** Validation, Writing – original draft. **Y. C. Fan:** Writing – review & editing. **Z. L. Wang:** Writing – review & editing, Funding acquisition. **X. Y. Lang:** Resources, Writing – review & editing, Supervision. **J. C. Li:** Resources, Writing – review & editing. **Q. Jiang:** Writing – review & editing, Funding acquisition, Project administration.

Declaration of Competing Interest

The authors declare that they have no known competing financial interests or personal relationships that could have appeared to influence the work reported in this paper.

Data Availability

Data will be made available on request.

Acknowledgments

The authors wish to thank National Natural Science Foundation of China (No. 52130101, 52271217), JLU Science and Technology Innovative Research Team and Science and Technology Research Project of the Education Department of Jilin Province (47120).

Appendix A. Supporting information

Supplementary data associated with this article can be found in the online version at doi:10.1016/j.apcatb.2023.123133.

References

- [1] X. Fu, J.B. Pedersen, Y. Zhou, M. Saccoccio, S. Li, R. Sazinas, K. Li, S.Z. Andersen, A. Xu, N.H. Deissler, J.B.V. Mygind, C. Wei, J. Kibsgaard, P.C.K. Vesborg, J. K. Nørskov, I. Chorkendorff, Continuous-flow electrosynthesis of ammonia by nitrogen reduction and hydrogen oxidation, *Science* 379 (2023) 707–712, <https://doi.org/10.1126/science.adf4403>.
- [2] G. Qing, R. Ghazfar, S.T. Jackowski, F. Habibzadeh, M.M. Ashtiani, C.P. Chen, M. R. Smith, T.W. Hamann, Recent advances and challenges of electrocatalytic N_2 reduction to ammonia, *Chem. Rev.* 120 (2020) 5437–5516, <https://doi.org/10.1021/acs.chemrev.9b00659>.

- [3] Y. Pang, C. Su, G. Jia, L. Xu, Z. Shao, Emerging two-dimensional nanomaterials for electrochemical nitrogen reduction, *Chem. Soc. Rev.* 50 (2021) 12744–12787, <https://doi.org/10.1039/d1cs00120e>.
- [4] S.L. Foster, S.I.P. Bakovic, R.D. Duda, S. Maheshwari, R.D. Milton, S.D. Minter, M. J. Janik, J.N. Renner, L.F. Greenlee, Catalysts for nitrogen reduction to ammonia, *Nat. Catal.* 1 (2018) 490–500, <https://doi.org/10.1038/s41929-018-0092-7>.
- [5] B.H.R. Suryanto, H.L. Du, D. Wang, J. Chen, A.N. Simonov, D.R. MacFarlane, Challenges and prospects in the catalysis of electroreduction of nitrogen to ammonia, *Nat. Catal.* 2 (2019) 290–296, <https://doi.org/10.1038/s41929-019-0252-4>.
- [6] H. Tao, C. Choi, L.X. Ding, Z. Jiang, Z. Hang, M. Jia, Q. Fan, Y. Gao, H. Wang, A. W. Robertson, S. Hong, Y. Jung, S. Liu, Z. Sun, Nitrogen fixation by Ru single-atom electrocatalytic reduction, *Chem* 5 (2019) 204–214, <https://doi.org/10.1016/j.chempr.2018.10.007>.
- [7] H. Shen, C. Choi, J. Masa, X. Li, J. Qiu, Y. Jung, Z. Sun, Electrochemical ammonia synthesis: mechanistic understanding and catalyst design, *Chem* 7 (2021) 1708–1754, <https://doi.org/10.1016/j.chempr.2021.01.009>.
- [8] W. Wu, C. Niu, P. Yan, F. Shi, C. Ma, X. Yang, Y. Jia, J. Chen, M.I. Ahmed, C. Zhao, Q. Xu, Building of sub-monolayer MoS_{2-x} structure to circumvent the scaling relations in N₂-to-NH₃ electrocatalysis, *Appl. Catal. B* 298 (2021), 120615, <https://doi.org/10.1016/j.apcatb.2021.120615>.
- [9] Z.W. Chen, Z. Lu, L.X. Chen, M. Jiang, D. Chen, C.V. Singh, Machine-learning-accelerated discovery of single-atom catalysts based on bidirectional activation mechanism, *Chem. Catal.* 1 (2021) 183–195, <https://doi.org/10.1016/j.checcat.2021.03.003>.
- [10] E. Skulason, T. Bligaard, S. Gudmundsdottir, F. Studt, J. Rossmeisl, F. Abild-Pedersen, T. Vegge, H. Jonsson, J.K. Nørskov, A theoretical evaluation of possible transition metal electrocatalysts for N₂ reduction, *Phys. Chem. Chem. Phys.* 14 (2012) 1235–1245, <https://doi.org/10.1039/c1cp22271f>.
- [11] G. Peng, J.W. Zhao, J. Wang, E. Hoenig, S. Wu, M. Wang, M. He, L. Zhang, J.X. Liu, C. Liu, Crystal structures of molybdenum borides dictate electrocatalytic ammonia synthesis efficiency, *Appl. Catal. B* 338 (2023), 123020, <https://doi.org/10.1016/j.apcatb.2023.123020>.
- [12] L. Huo, X. Han, L. Zhang, B. Liu, R. Gao, B. Cao, W.W. Wang, C.J. Jia, K. Liu, J. Liu, J. Zhang, Spatial confinement and electron transfer moderating Mo-N bond strength for superior ammonia decomposition catalysis, *Appl. Catal. B* 294 (2021), 120254, <https://doi.org/10.1016/j.apcatb.2021.120254>.
- [13] Y. Ma, T. Yang, H. Zou, W. Zang, Z. Kou, L. Mao, Y. Feng, L. Shen, S.J. Pennycook, L. Duan, X. Li, J. Wang, Synergizing Mo single atoms and Mo₂C nanoparticles on CNTs synchronizes selectivity and activity of electrocatalytic N₂ reduction to ammonia, *Adv. Mater.* 32 (2020) 2002177, <https://doi.org/10.1002/adma.202002177>.
- [14] H. Fei, T. Guo, Y. Xin, L. Wang, R. Liu, D. Wang, F. Liu, Z. Wu, Sulfur vacancy engineering of MoS₂ via phosphorus incorporation for improved electrocatalytic N₂ reduction to NH₃, *Appl. Catal. B* 300 (2022), 120733, <https://doi.org/10.1016/j.apcatb.2021.120733>.
- [15] K. Chu, Y. Luo, P. Shen, X. Li, Q. Li, Y. Guo, Unveiling the synergy of O-vacancy and heterostructure over MoO_{3-x}/MXene for N₂ electroreduction to NH₃, *Adv. Energy Mater.* 12 (2021) 2103022, <https://doi.org/10.1002/aenm.202103022>.
- [16] J.H. Montoya, C. Tsai, A. Vojvodic, J.K. Nørskov, The challenge of electrochemical ammonia synthesis: A new perspective on the role of nitrogen scaling relations, *ChemSusChem* 8 (2015) 2180–2186, <https://doi.org/10.1002/cssc.201500322>.
- [17] C.N. Sun, Z.L. Wang, X.Y. Lang, Z. Wen, Q. Jiang, Synergistic effect of active sites of double-atom catalysts for nitrogen reduction reaction, *ChemSusChem* 14 (2021) 4593–4600, <https://doi.org/10.1002/cssc.202101507>.
- [18] N.R. Singstock, C.B. Musgrave, How the bioinspired Fe₂Mo₆S₈ chevreol breaks electrocatalytic nitrogen reduction scaling relations, *J. Am. Chem. Soc.* 144 (2022) 12800–12806, <https://doi.org/10.1021/jacs.2c03661>.
- [19] R. Liu, H. Fei, J. Wang, T. Guo, F. Liu, J. Wang, Z. Wu, D. Wang, Insights of active sites separation mechanism for highly efficient electrocatalytic N₂ reduction to ammonia over glucose-induced metallic MoS₂, *Appl. Catal. B* 337 (2023) 12997, <https://doi.org/10.1016/j.apcatb.2023.122997>.
- [20] Y. Gong, J. Wu, M. Kitano, J. Wang, T.N. Ye, J. Li, Y. Kobayashi, K. Kishida, H. Abe, Y. Niwa, H. Yang, T. Tada, H. Hosono, Ternary intermetallic LaCoSi as a catalyst for N₂ activation, *Nat. Catal.* 1 (2018) 178–185, <https://doi.org/10.1038/s41929-017-0022-0>.
- [21] H. Yin, Z. Chen, S. Xiong, J. Chen, C. Wang, R. Wang, Y. Kuwahara, J. Luo, H. Yamashita, Y. Peng, J. Li, Alloying effect-induced electron polarization drives nitrate electroreduction to ammonia, *Chem. Catalysis* 1 (2021) 1088–1103, <https://doi.org/10.1016/j.checcat.2021.08.014>.
- [22] G. Fan, W. Xu, J. Li, J.L. Chen, M. Yu, Y. Ni, S. Zhu, X.C. Su, F. Cheng, Nanoporous NiSb to enhance nitrogen electroreduction via tailoring competitive adsorption sites, *Adv. Mater.* 33 (2021) 2101126, <https://doi.org/10.1002/adma.202101126>.
- [23] X. Wang, M. Luo, J. Lan, M. Peng, Y. Tan, Nanoporous intermetallic Pd₃Bi for efficient electrochemical nitrogen reduction, *Adv. Mater.* 33 (2021) 2007733, <https://doi.org/10.1002/adma.202007733>.
- [24] Y. Cui, A. Dong, Y. Qu, J. Zhang, M. Zhao, Z. Wang, Q. Jiang, Theory-guided design of nanoporous CuMn alloy for efficient electrocatalytic nitrogen reduction to ammonia, *Chem. Eng. J.* 426 (2021), 131843, <https://doi.org/10.1016/j.cej.2021.131843>.
- [25] T.N. Ye, S.W. Park, Y. Lu, J. Li, M. Sasase, M. Kitano, T. Tada, H. Hosono, Vacancy-enabled N₂ activation for ammonia synthesis on an Ni-loaded catalyst, *Nature* 583 (2020) 391–395, <https://doi.org/10.1038/s41586-020-2464-9>.
- [26] G. Kresse, J. Furthmüller, Efficiency of ab-initio total energy calculations for metals and semiconductors using a plane-wave basis set, *Comput. Mater. Sci.* 6 (1996) 15–50, [https://doi.org/10.1016/0927-0256\(96\)00008-0](https://doi.org/10.1016/0927-0256(96)00008-0).
- [27] J.F.G. Kresse, Efficient iterative schemes for ab initio total-energy calculations using a plane-wave basis set, *Phys. Rev. B* 54 (1996) 11169–11186, <https://doi.org/10.1103/PhysRevB.54.11169>.
- [28] P.E. Blöchl, Projector augmented-wave method, *Phys. Rev. B* 50 (1994) 17953–17979, <https://doi.org/10.1103/PhysRevB.50.17953>.
- [29] D.J.G. Kresse, From ultrasoft pseudopotentials to the projector augmented-wave method, *Phys. Rev. B* 59 (1999) 1758–1775, <https://doi.org/10.1103/PhysRevB.59.1758>.
- [30] J.P. Perdew, K. Burke, M. Ernzerhof, Generalized gradient approximation made simple, *Phys. Rev. Lett.* 77 (1996) 3865–3868, <https://doi.org/10.1103/PhysRevLett.77.3865>.
- [31] S. Grimme, S. Ehrlich, L. Goerigk, Effect of the damping function in dispersion corrected density functional theory, *J. Comput. Chem.* 32 (2011) 1456–1465, <https://doi.org/10.1002/jcc.21759>.
- [32] X. Guo, J. Gu, S. Lin, S. Zhang, Z. Chen, S. Huang, Tackling the activity and selectivity challenges of electrocatalysts toward the nitrogen reduction reaction via atomically dispersed biatom catalysts, *J. Am. Chem. Soc.* 142 (2020) 5709–5721, <https://doi.org/10.1021/jacs.9b13349>.
- [33] L. Li, J.M.P. Martinez, E.A. Carter, Prediction of highly selective electrocatalytic nitrogen reduction at low overpotential on a Mo-doped g-GaN monolayer, *ACS Catal.* 10 (2020) 12841–12857, <https://doi.org/10.1021/acscatal.0c03140>.
- [34] S. Maintz, V.L. Deringer, A.L. Tchougreff, R. Dronskowski, Lobster: a tool to extract chemical bonding from plane-wave based DFT, *J. Comput. Chem.* 37 (2016) 1030–1035, <https://doi.org/10.1002/jcc.24300>.
- [35] J.K. Nørskov, J. Rossmeisl, A. Logadottir, L. Lindqvist, J.R. Kitchin, T. Bligaard, H. Jónsson, Origin of the overpotential for oxygen reduction at a fuel-cell cathode, *J. Phys. Chem. B* 108 (2004) 17886–17892, <https://doi.org/10.1021/jp047349j>.
- [36] W.M. Haynes (Ed.), *CRC Handbook of Chemistry and Physics*, CRC Press, Taylor and Francis, Boca Raton, FL, 2016, p. 876.
- [37] A.R. Singh, B.A. Rohr, J.A. Schwalbe, M. Cargnello, K. Chan, T.F. Jaramillo, I. Chorkendorff, J.K. Nørskov, Electrochemical ammonia synthesis—the selectivity challenge, *ACS Catal.* 7 (2016) 706–709, <https://doi.org/10.1021/acscatal.6b03035>.
- [38] W. Guo, K. Zhang, Z. Liang, R. Zou, Q. Xu, Electrochemical nitrogen fixation and utilization: theories, advanced catalyst materials and system design, *Chem. Soc. Rev.* 48 (2019) 5658–5716, <https://doi.org/10.1039/c9cs00159j>.
- [39] Z. Wei, Z. Gu, Y. Zhang, K. Luo, S. Zhao, Phase-separated CuAg alloy interfacial stress induced Cu defects for efficient N₂ activation and electrocatalytic reduction, *Appl. Catal. B* 320 (2023), 121915, <https://doi.org/10.1016/j.apcatb.2022>.
- [40] V. Shadravan, A.N.G. Cao, V.J. Bukas, M.K. Gronborg, C.D. Damsgaard, Z. Wang, J. Kibsgaard, J.K. Nørskov, I. Chorkendorff, Enhanced promotion of Ru-based ammonia catalysts by in situ dosing of Cs, *Energy Environ. Sci.* (2022), <https://doi.org/10.1039/d2ee00591c>.
- [41] X. Li, T. Li, Y. Ma, Q. Wei, W. Qiu, H. Guo, X. Shi, P. Zhang, A.M. Asiri, L. Chen, B. Tang, X. Sun, Boosted electrocatalytic N₂ reduction to NH₃ by defect-rich MoS₂ nanoflower, *Energy Mater.* 8 (2018) 1801357, <https://doi.org/10.1002/aenm.201801357>.
- [42] G.W. Watt, J.D. Chrisp, Spectrophotometric method for determination of hydrazine, *Anal. Chem.* 24 (1952) 2006–2008, <https://doi.org/10.1021/ac60072a044>.
- [43] S. Liu, T. Qian, M. Wang, H. Ji, X. Shen, C. Wang, C. Yan, Proton-filtering covalent organic frameworks with superior nitrogen penetration flux promote ambient ammonia synthesis, *Nat. Catal.* 4 (2021) 322–331, <https://doi.org/10.1038/s41929-021-00599-w>.
- [44] W. Gao, Y. Chen, B. Li, S.P. Liu, X. Liu, Q. Jiang, Determining the adsorption energies of small molecules with the intrinsic properties of adsorbates and substrates, *Nat. Commun.* 11 (2020) 1196, <https://doi.org/10.1038/s41467-020-14969-8>.
- [45] Z.W. Chen, Z. Garipey, L. Chen, X. Yao, A. Anand, S.J. Liu, C.G. Tetsassi Feugmo, I. Tamblin, C.V. Singh, Machine-learning-driven high-entropy alloy catalyst discovery to circumvent the scaling relation for CO₂ reduction reaction, *ACS Catal.* 12 (2022) 14864–14871, <https://doi.org/10.1021/acscatal.2c03675>.
- [46] N. Kulo, S. He, W. Ecker, R. Pippan, T. Antretter, V.I. Razumovskiy, Thermodynamic and mechanical stability of Ni₃X-type intermetallic compounds, *Intermetallics* 114 (2019), 106604, <https://doi.org/10.1016/j.intermet.2019.106604>.
- [47] M.Y. Zu, C. Wang, L. Zhang, L.R. Zheng, H.G. Yang, Reconstructing bimetallic carbide Mo₆Ni₆C for carbon interconnected MoNi alloys to boost oxygen evolution electrocatalysis, *Mater. Horiz.* 6 (2019) 115–121, <https://doi.org/10.1039/c8mh00664d>.
- [48] H.Y. Zhou, Y.B. Qu, J.C. Li, Z.L. Wang, C.C. Yang, Q. Jiang, Effectively boosting selective ammonia synthesis on electron-deficient surface of MoB₂, *Appl. Catal. B* 305 (2021), 121023, <https://doi.org/10.1016/j.apcatb.2021.121023>.
- [49] X. Lv, W. Wei, B. Huang, Y. Dai, T. Frauenheim, High-throughput screening of synergistic transition metal dual-atom catalysts for efficient nitrogen fixation, *Nano Lett.* 21 (2021) 1871–1878, <https://doi.org/10.1021/acs.nanolett.0c05080>.
- [50] S. Han, X. Wei, Y. Huang, J. Zhang, J. Yang, Z. Wang, Tuning the activity and selectivity of nitrogen reduction reaction on double-atom catalysts by B doping: a density functional theory study, *Nano Energy* 99 (2022), 107363, <https://doi.org/10.1016/j.nanoen.2022.107363>.
- [51] X. Wang, S. Qiu, J. Feng, Y. Tong, F. Zhou, Q. Li, L. Song, S. Chen, K.H. Wu, P. Su, S. Ye, F. Hou, S.X. Dou, H.K. Liu, G.Q. Lu, C. Sun, J. Liu, J. Liang, Confined Fe-Cu clusters as sub-nanometer reactors for efficiently regulating the electrochemical nitrogen reduction reaction, *Adv. Mater.* 32 (2020) 2004382, <https://doi.org/10.1002/adma.202004382>.

- [52] X. Li, P. Shen, Y. Luo, Y. Li, Y. Guo, H. Zhang, K. Chu, PdFe single-atom alloy metallene for N_2 electroreduction, *Angew. Chem. Int. Ed.* 61 (2022), e202205923, <https://doi.org/10.1002/anie.202205923>.
- [53] Y. Li, Y. Ji, Y. Zhao, J. Chen, S. Zheng, X. Sang, B. Yang, Z. Li, L. Lei, Z. Wen, X. Feng, Y. Hou, Local spin-state tuning of iron single-atom electrocatalyst by S-coordinated doping for kinetics-boosted ammonia synthesis, *Adv. Mater.* 34 (2022) 2202240, <https://doi.org/10.1002/adma.202202240>.
- [54] P. Shen, X. Li, Y. Luo, Y. Guo, X. Zhao, K. Chu, High-efficiency N_2 electroreduction enabled by Se-vacancy-rich WSe_{2-x} in water-in-salt electrolytes, *ACS Nano* 16 (2022) 7915–7925, <https://doi.org/10.1021/acsnano.2c00596>.
- [55] X. Wang, Y. Zhao, L. Wang, W. Peng, J. Feng, D. Li, B.J. Su, J.Y. Juang, Y. Ma, Y. Chen, F. Hou, S. Zhou, H.K. Liu, S.X. Dou, J. Liu, J. Liang, Regulating the electronic configuration of supported iron nanoparticles for electrochemical catalytic nitrogen fixation, *Adv. Funct. Mater.* 32 (2022) 2111733, <https://doi.org/10.1002/adfm.202111733>.
- [56] Y. Zhang, Q. Zhang, D.-X. Liu, Z. Wen, J.X. Yao, M.M. Shi, Y.F. Zhu, J.M. Yan, Q. Jiang, High spin polarization ultrafine Rh nanoparticles on CNT for efficient electrochemical N_2 fixation to ammonia, *Appl. Catal. B* 298 (2021), 120592, <https://doi.org/10.1016/j.apcatb.2021.120592>.
- [57] M. Yuan, Q. Li, J. Zhang, J. Wu, T. Zhao, Z. Liu, L. Zhou, H. He, B. Li, G. Zhang, Engineering surface atomic architecture of NiTe nanocrystals toward efficient electrochemical N_2 fixation, *Adv. Funct. Mater.* 30 (2020) 2004208, <https://doi.org/10.1002/adfm.202004208>.
- [58] C. Choi, G.H. Gu, J. Noh, H.S. Park, Y. Jung, Understanding potential-dependent competition between electrocatalytic dinitrogen and proton reduction reactions, *Nat. Commun.* 12 (2021) 4353, <https://doi.org/10.1038/s41467-021-24539-1>.
- [59] D. Wang, C. Han, Z. Xing, Q. Li, X. Yang, Pt-like catalytic behavior of MoNi decorated $CoMoO_3$ cuboid arrays for the hydrogen evolution reaction, *J. Mater. Chem. A* 6 (2018) 15558–15563, <https://doi.org/10.1039/C8TA04391D>.
- [60] M. Wang, H. Yang, J. Shi, Y. Chen, Y. Zhou, L. Wang, S. Di, X. Zhao, J. Zhong, T. Cheng, W. Zhou, Y. Li, Alloying nickel with molybdenum significantly accelerates alkaline hydrogen electrocatalysis, *Angew. Chem. Int. Ed.* 60 (2021) 5771–5777, <https://doi.org/10.1002/anie.202013047>.
- [61] J. Zhang, X. Tian, M. Liu, H. Guo, J. Zhou, Q. Fang, Z. Liu, Q. Wu, J. Lou, Cobalt-modulated molybdenum–dinitrogen interaction in MoS_2 for catalyzing ammonia synthesis, *J. Am. Chem. Soc.* 141 (2019), <https://doi.org/10.1021/jacs.9b02501>.
- [62] Y. Zeng, Y. Meng, Z. Lai, X. Zhang, M. Yu, P. Fang, M. Wu, Y. Tong, X. Lu, An ultrastable and high-performance flexible fiber-shaped Ni–Zn battery based on a Ni–NiO heterostructured nanosheet cathode, *Adv. Mater.* 29 (2017) 1702698, <https://doi.org/10.1002/adma.201702698>.
- [63] C. Tang, S.Z. Qiao, How to explore ambient electrocatalytic nitrogen reduction reliably and insightfully, *Chem. Soc. Rev.* 48 (2019) 3166–3180, <https://doi.org/10.1039/c9cs00280d>.
- [64] Y. Luo, Z. Zhang, M. Chhowalla, B. Liu, Recent advances in design of electrocatalysts for high-current-density water splitting, *Adv. Mater.* 34 (2022), e2108133, <https://doi.org/10.1002/adma.202108133>.
- [65] D. Yao, C. Tang, L. Li, B. Xia, A. Vasileff, H. Jin, Y. Zhang, S.Z. Qiao, In situ fragmented bismuth nanoparticles for electrocatalytic nitrogen reduction, *Adv. Energy Mater.* 10 (2020), <https://doi.org/10.1002/aenm.202001289>.
- [66] H. Yan, N. Zhang, D. Wang, Highly efficient CeO_2 -supported noble-metal catalysts: From single atoms to nanoclusters, *Chem. Catal.* 2 (2022) 1594–1623, <https://doi.org/10.1016/j.checat.2022.05.001>.
- [67] M. Zhang, P. Zou, G. Jeerh, B. Sun, M. Walker, S. Tao, Oxygen vacancy-rich $La_{0.5}Sr_{1.5}Ni_{0.9}Cu_{0.1}O_{4-\delta}$ as a high-performance bifunctional catalyst for symmetric ammonia electrolyzer, *Adv. Funct. Mater.* 32 (2022) 2204881, <https://doi.org/10.1002/adfm.202204881>.
- [68] H. Fei, R. Liu, J. Wang, T. Guo, Z. Wu, D. Wang, F. Liu, Targeted modulation of competitive active sites toward nitrogen fixation via sulfur vacancy engineering over MoS_2 , *Adv. Funct. Mater.* (2023) 2302501, <https://doi.org/10.1002/adfm.202302501>.
- [69] D. Zhang, H. Zhao, X. Wu, Y. Deng, Z. Wang, Y. Han, H. Li, Y. Shi, X. Chen, S. Li, J. Lai, B. Huang, L. Wang, Multi-site electrocatalysts boost ph-universal nitrogen reduction by high-entropy alloys, *Adv. Funct. Mater.* 31 (2021) 2006939, <https://doi.org/10.1002/adfm.202006939>.